Nanoelectronics and Its New Materials – A NEW ERA OF NANOSCIENCE

Nanoelectronics and Its New Materials –
A NEW ERA OF NANOSCIENCE

ZEISS
Seeing beyond

WILEY

Discover the recent advances in electronics research and fundamental nanoscience.

Nanotechnology has become the driving force behind breakthroughs in engineering, materials science, physics, chemistry, and biological sciences. In this compendium, we delve into a wide range of novel applications that highlight recent advances in electronics research and fundamental nanoscience. From surface analysis and defect detection to tailored optical functionality and transparent nanowire electrodes, this eBook covers key topics that will revolutionize the future of electronics.

To get your hands on this valuable resource and unleash the power of nanotechnology, simply download the eBook now. Stay ahead of the curve and embrace the future of electronics with nanoscience as your guide.

ZEISS

Seeing beyond

WILEY

A Guideline to Mitigate Interfacial Degradation Processes in Solid-State Batteries Caused by Cross Diffusion

Mir Mehraj Ud Din, Lukas Ladenstein, Joseph Ring, Daniel Knez, Stefan Smetaczek, Markus Kubicek, Mohsen Sadeqi-Moqadam, Steffen Ganschow, Elena Salagre, Enrique G. Michel, Stefanie Lode, Gerald Kothleitner, Iulian Dugulan, Jeffrey G. Smith, Andreas Limbeck, Jürgen Fleig, Donald J. Siegel, Günther J. Redhammer, and Daniel Rettenwander*

Dedicated to Prof. Georg Amthauer on 80st birthday

Diffusion of transition metals across the cathode–electrolyte interface is identified as a key challenge for the practical realization of solid-state batteries. This is related to the formation of highly resistive interphases impeding the charge transport across the materials. Herein, the hypothesis that formation of interphases is associated with the incorporation of Co into the Li$_7$La$_3$Zr$_2$O$_{12}$ lattice representing the starting point of a cascade of degradation processes is investigated. It is shown that Co incorporates into the garnet structure preferably four-fold coordinated as Co^{2+} or Co^{3+} depending on oxygen fugacity. The solubility limit of Co is determined to be around 0.16 per formula unit, whereby concentrations beyond this limit causes a cubic-to-tetragonal phase transition. Moreover, the temperature-dependent Co diffusion coefficient is determined, for example, $D_{700\,°C} = 9.46 \times 10^{-14}$ cm^2 s^{-1} and an activation energy $E_a = 1.65$ eV, suggesting that detrimental cross diffusion will take place at any relevant process condition. Additionally, the optimal protective Al$_2$O$_3$ coating thickness for relevant temperatures is studied, which allows to create a process diagram to mitigate any degradation with a minimum compromise on electrochemical performance. This study provides a tool to optimize processing conditions toward developing high energy density solid-state batteries.

1. Introduction

Solid-state batteries (SSBs) are considered as a key technology for the development of affordable and versatile electrical vehicles with extended driving ranges and improved safety. The main advantage originates from the adoption of a solid electrolyte instead of a flammable organic liquid. Moreover, solid electrolytes enable the integration of Li metal or its alloys enabling ultimately high energy densities. However, to reach the promised performance of solid-state batteries suitable solid electrolytes needs to be developed. For example, polymer-based electrolytes can enable cheap production of SSBs by allowing current role-to-role technology; however, the low conductivity of polymer electrolytes requires temperatures above 50 °C to provide sufficient cycling performance. Furthermore, due to their organic nature, safety remains an issue. Sulfide-based electrolytes show among the highest Li-ion conductivities ensuring

M. M. U. Din, M. Sadeqi-Moqadam, D. Rettenwander
Department of Material Science and Engineering
NTNU Norwegian University of Science and Technology
Trondheim 7034, Norway
E-mail: daniel.rettenwander@ntnu.no

M. M. U. Din, D. Rettenwander
Christian Doppler Laboratory for Solid-State Batteries
NTNU Norwegian University of Science and Technology
Trondheim 7034, Norway

M. M. U. Din, L. Ladenstein, D. Rettenwander
Institute of Chemistry and Technology of Materials
Graz University of Technology
Graz 8010, Austria

J. Ring, S. Smetaczek, M. Kubicek, A. Limbeck, J. Fleig
Institute of Chemical Technologies and Analytics
TU Wien
Wien 1060, Austria

D. Knez, S. Ganschow, G. Kothleitner
Institute of Electron Microscopy and Nanoanalysis and Graz Centre for Electron Microscopy
Graz University of Technology
Graz 8010, Austria

satisfying rate capability of the respective SSB, but their instability versus high and low voltage electrodes is a drawback with respect to energy density. Halides have high Li-ion conductivity and possess good stability against high-voltage cathodes but are limited by their instability against Li metal anodes. Oxide-based Li-ion conductors, such as $Li_7La_3Zr_2O_{12}$ and variants (LLZO; see structural details in **Figure 1**a)[1–3] belong to the most promising candidates, due to their unique feature of combining electrochemical stability with relatively high Li-ion conductivities (up to 1.3 mScm^{-1}) with the potential to enable SSBs with theoretical energy densities of up to >400 Wh kg^{-1} and >1000 Wh L^{-1}.[4–6] Further advantages of LLZO are its processibility in air, and improved safety even at high operating temperatures compared to other solid electrolytes.

Despite the promising prerequisites of LLZO, its integration into a battery is associated with the formation of complex solid-to-solid interfaces that arise as the main bottlenecks to achieve high power density, rate capacity, and capacity retention of SSBs, which impede their ultimate commercial usage.[7,8] Whereas for the Li | LLZO interface significant improvements have been achieved,[9] the cathode side still suffers from technical challenges such as poor contact between the LLZO and the cathode or contact loss during cycling due to volume changes within the cathode.[10–14] A stable interface contact is a key requirement for high initial discharge capacities, this however, requires high temperature processing. To form sufficient bonding between the individual components in an all-oxide cathode composed by LLZO

D. Knez
Leibniz-Institut für Kristallzüchtung
12489 Berlin, Germany

E. Salagre, E. G. Michel
Departamento de Física de la Materia Condensada
Facultad de Ciencias
Universidad Autónoma de Madrid
Madrid E-28049, Spain

E. Salagre, E. G. Michel
Condensed Matter Physics Center (IFIMAC)
Universidad Autónoma de Madrid
Madrid E-28049, Spain

S. Lode
Department of Geoscience and Petroleum
Norwegian University of Science and Technology
Trondheim 7031, Norway

I. Dugulan
Fundamental Aspects Mat and Energy Group
Delft University of Technology
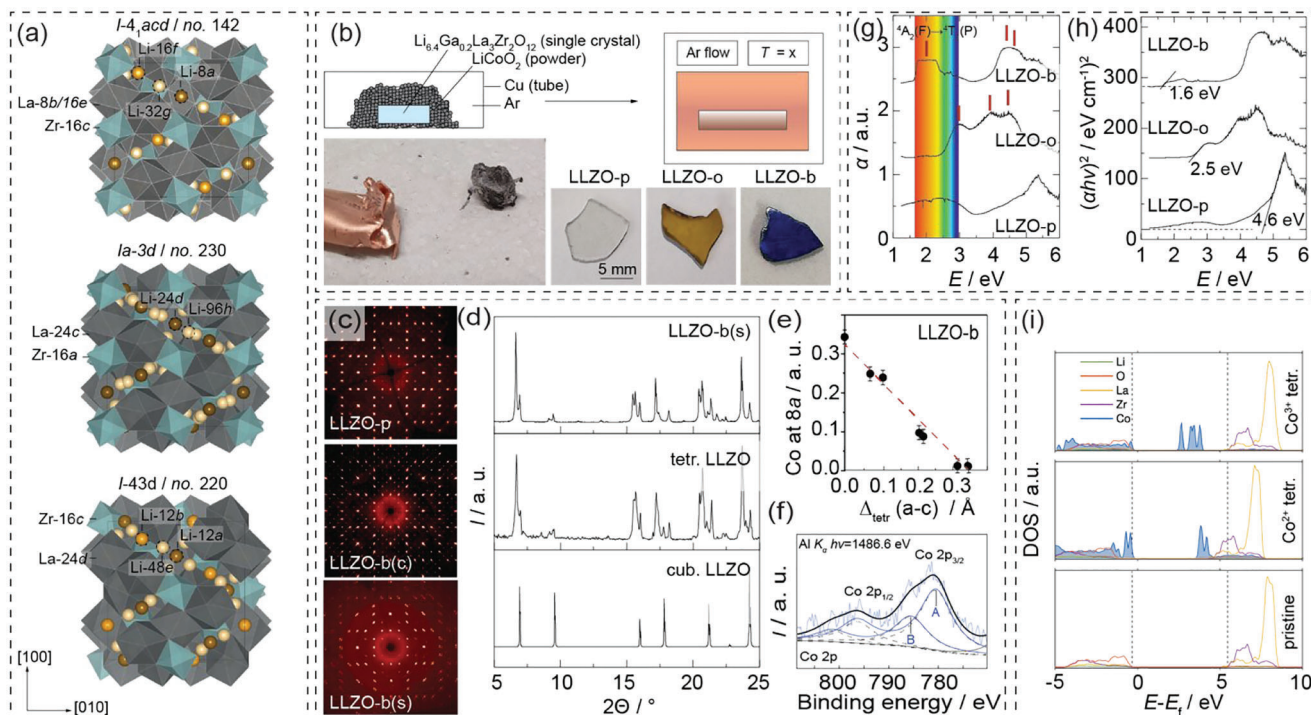Mekelweg 15, Delft 2629 JB, the Netherlands

J. G. Smith, D. J. Siegel
Mechanical Engineering Department
University of Michigan
Ann Arbor, MI 48109, USA

J. G. Smith, D. J. Siegel
Walker Department of Mechanical Engineering
Texas Materials Institute
Oden Institute for Computational Engineering
and Sciences, and Joint Center for Energy Storage Research
University of Texas at Austin
Austin, TX 78712-1591, USA

G. J. Redhammer
Department of Chemistry and Physics of Materials
University of Salzburg
Salzburg 5020, Austria

and $LiCoO_2$ (LCO) temperatures from 600 to 1050 °C are required (see **Table 1**).

High temperatures, however, result in mutual diffusion and interfacial reactions between the solid electrolytes and the electrode leading to the formation of an insulating degradation layer, which is detrimental for the performance of an SSB. For example, the state-of-the-art cell composed of composite cathode based on LLZO, LCO, and a sinter additive has been shown to suffer from very high interfacial resistance (270 Ω cm^2 at 100 °C), which is predominantly attributed to the high processing temperature of 700 °C.[15] Such values are too high to achieve a target cycling at 1 C with more than 90% efficiency; values as low as 40 Ω cm^2 are required.[16]

The underlying processes taking place at the interface during cell fabrication were intensively studied previously. For example, Kim et al.[17] deposited 100 nm thick LCO films on LLZO by pulse laser deposition at 650 °C for 1 h and observed La/Co cross diffusion along the interface between LLZO and LCO accompanied by the formation of La_2CoO_4 phase. Vadar et al.[18] additionally observed the formation of other poor conducting phases, such as Li_2CO_3, $La_2Zr_2O_7$, and $LaCoO_3$. Park et al.[19] mixed LLZO and LCO powders to study the phase stability as a function of temperature via X-ray diffraction (XRD) observing a structural degradation by the formation of the tetragonal LLZO phase. Since the tetragonal phase has a lower Li-ion conductivity a detrimental effect on the interfacial transport properties can be expected. The authors relate the lowering in symmetry to a loss of Al during the heat treatment (Note: supervalent cations are needed to stable the high conductive cubic phase of LLZO at RT, hence, the loss of Al will consequently lead to the tetragonal phase).[19] The formation of the tetragonal phase can also be associated with the loss of Li in LLZO at elevated temperatures leading to the formation of non-conductive phases, that is, $La_2Zr_2O_7$ and La_2O_3.[20] These decomposition products have also been computationally predicted to form when LLZO is in contact with delithiated LCO.[21]

Recently, Ren et al.[22] highlighted that the disagreement on the reaction products and their onset formation temperature could originate from different specific processing conditions and thus cannot be accurately predicted solely by thermodynamic considerations. Authors suggest that kinetics must be considered to understand the reactions occurring at the interfaces. This requires detailed knowledge on cross diffusion of ions and formation of the passivation layer between cathode and LLZO at a given temperature. Such knowledge is, however, not available so far.

Despite the formation of interphases related to the decomposition of LLZO the sole incorporation of a transition metal into the garnet structure could have significant structural and electrochemical consequences; studies in this respect are, however, absent. For example, the incorporation of Fe has been demonstrated to enable Li-ion conductivities up to 1.3 mS cm^{-1}; but the incorporation of 3d-electronic states can also cause electronic conduction. The later one could be beneficial when used as a catholyte, but detrimental when used as a separator. Moreover, additional electronic states in the band gap can lower the electrochemical stability, hence limits its application toward high voltage cathodes.

Considering the potential implications of Co on LLZO, in-depth studies are needed to understand the role of Co in the

**ADVANCED
SCIENCE NEWS**

www.advancedsciencenews.com

**ADVANCED
FUNCTIONAL
MATERIALS**

www.afm-journal.de

Figure 1. a) LLZO garnets can crystallize in highly conductive cubic modifications, a centric cubic space group (Ia-3d, no. 230) and an acentric cubic space group (I-43d, no. 220), and a less conductive tetragonal polymorph (SG: I41/acd, no. 142). The former is stabilized at room temperature by supervalent substitution at the Li, La, or Zr position in LLZO. b) Selected LLZO samples before and after annealing in LCO powder and subsequent removal by polishing. c) Recalculated precession images of the hk0 layer in LLZO-p, LLZO-b(c) and LLZO-b(s). Note the much more intense superstructure, obeying the Ia-3d symmetry in the picture of LLZO-b(c). Simulated precession image of the 0kl layer of LLZO-b(s) shows multiple twinning (Vierling). d) Corresponding powder XRD diffraction pattern of LLZO-b in comparison to tetragonal and cubic LLZO serving as the reference. Clear phase transformation to tetragonal LLZO-b is observed. e) Change in the lattice parameter with increasing Co content in LLZO-b. f) XPS Co 2p core level spectra for sample LLZO-b with peak deconvolution in a main component (A) and a satellite (B). The energy shift of B is typical of Co^{2+}. g,h) Optical absorption spectra (g) and corresponding Tauc plot (h) of LLZO-p, LLZO-o, and LLZO-b. i) Partial density of states of cubic (I-43d) LLZO, undoped, and Co^2 or Co^{3+}-doped on tetrahedral sites (12a).

degradation processes at high temperature to develop contingency strategies for safe processing of SSBs. The questions to be answered are:

Does Co incorporate into the LLZO structure? If so, to which extent, which site does it occupy and in which oxidation state? What are the consequences in respect of structure, ionic and electronic conductivity, as well as electrochemical stability?

Furthermore, if Co has an impact on the performance of LLZO, at which concentration does it get detrimental and when is this critical Co concentration in the interfacial region been reached, considering annealing temperature and time?

To answer these questions, we chose two approaches to incorporate Co, 1) large LLZO single crystals have been embedded into LCO powders or 2) LCO has been deposited by RF magnetron sputtering followed by heat treatments. A continuum of characterization techniques has been applied to gain structural (i.e., powder (P) and single crystal (SC) XRD, electron diffraction, UV–vis spectroscopy, ^{57}Co Emission Mössbauer spectroscopy, and X-ray photo emission spectroscopy (XPS)), chemical (e.g., inductive coupled plasma optical emission spectroscopy (ICP-OES) and time-of-flight secondary ion mass spectroscopy (TOF-SIMS)), microstructural (e.g., scanning electron microscopy (SEM) and transmission electron microscopy (TEM)), electrical (i.e., impedance spectroscopy and polarization experiments), and electrochemical (i.e., CV) insights supported by DFT and finite element analysis. Finally, we have been able to show that Co can incorporate into the garnet structure with significant impact on the structural, microstructural, and electrochemical properties. Moreover, the temperature-dependent Co diffusion coefficient in LLZO has been determined, which allowed for the creation of a process diagram suggesting the optimal Al_2O_3 coating thickness for any conditions that keeps degradation during processing at a minimum to negate the impact on cell performance.

2. Results and Discussion

2.1. Optical Inspection

To incorporate different amounts of Co, LLZO single crystal was embedded in LCO powder inside a Cu tube (see Figure 1b). The tube was then sealed under vacuum and heat treated at different temperatures and dwelling times under Ar to avoid Cu oxidation. After the heat treatment, the embedded single crystals were

Table 1. Summary of previous studies on the thermal interfacial stability of garnet-type solid electrolytes and $LiCoO_2$.

Composition[a]	Formation method	Onset reaction T [°C]	Reaction products
$Li_6BaLa_2Ta_2O_{12}$	powder	< =900	Non detected
$Li_7La_{2.75}Ca_{0.25}Zr_{1.75}Ta_{0.25}O_{12}$	PVD	800	tetragonal $Li_7La_3Zr_2O_{12}$
$Li_{6.75}La_3Zr_{1.75}Ta_{0.25}O_{12}$	powder	500–600	$La_2Zr_2O_7$
	powder	600–700	$LaCoO_3$
$Li_{6.75}La_3Zr_{1.75}Nb_{0.25}O_{12}$	PVD	>600	Non detected
Al_2O_3-added LLZO	PVD	>500	Non detected
Al-doped $Li_7La_3Zr_2O_{12}$	powder	700	tetragonal $Li_7La_3Zr_2O_{12}$
$Li_{6.25}Al_{0.25}La_3Zr_2O_{12}$	powder	>800	Non detected
Al-doped $Li_7La_3Zr_2O_{12}$	PVD	<300	$LaCoO_3$, $La_2Zr_2O_7$, Li_2CO_3
$Li_{6.25}Ga_{0.25}La_3Zr_2O_{12}$	PVD	700	$La_2Zr_2O_7$
$Li_7La_3Zr_2O_{12}$	PVD	700	La_2CoO_4
tetragonal $Li_7La_3Zr_2O_{12}$	powder	600	$La_2Li_{0.5}Co_{0.5}O_4$

[a] Table adapted from Ref. [9]; powder: LLZO:CAT mixture or CAT powder casted on LLZO; PVD: either CAT deposited on LLZO via PLD or RF magnetron sputtering.

covered in a solid coating being surrounded by a metallic-appearing surface, which was removed by sanding. After removing the LCO coating, single crystals were recovered with colors ranging from almost transparent to blue depending on the treatment history (see Figure 1b). All single crystals revealed a uniform distribution of the color throughout the whole samples, whereas blue LLZO (LLZO-b) showed also dark blue spots and pale-greenish rim (before polishing.; not visible in Figure 1b). For further analysis pristine (LLZO-p), orange (LLZO-o) (5 days at 500 °C), and blue LLZO-b (5 days at 900 °C) LLZO single crystals were considered.

Such color changes have been observed previously for LLZO mixed with LCO and annealed at temperatures above 600 °C. Moreover, it has been shown that samples tend to become more greenish when higher temperatures are applied.[22] Based on observations made on garnet analogs the color changes could be associated with the incorporation of Co, for example, Co^{2+} on the tetrahedral side (Wykoff position 24d in cubic garnets with space group $Ia\bar{3}d$). In the $Ca_3Sb_2Fe_2Zn_{1-x}Co_xO_{12}$ ($0 \leq x \leq 1.0$) system, the incorporation of Co^{2+} on the 24d site causes a change from yellowish, turquoise green to intense green color.[23] Color variations from white, sky blue to dark blue have also been observed in the $Ca_3Sb_2Ga_2Zn_{1-x}Co_xO_{12}$ ($0<x\leq1.0$) system. A dark blue and intense color is reported in other crystals systems, for example, spinels or silicates such as Co-akermannite $Ca_2CoSi_2O_7$,[24] when Co^{2+} occupies tetrahedral position. Pale green color changes were reported for high purity Co-doped garnets, that is, $Y_3Fe_5O_{12}$, $Y_3Ga_5O_{12}$, and $Y_3Al_5O_{12}$ with $Ia\bar{3}d$ symmetry with mainly Co^{3+} and minor amounts of Co^{2+} occupying tetrahedral sites.[25] Color changes—in comparison with literature observations—may indicate the presence of Co in tetrahedral coordination. A change from orange to dark blue in dependence on temperature additionally may indicate a change in valence state due to changing oxygen fugacity with Co2+ stabilized at higher temperatures (dark blue samples). Further evidence on the influence of the oxygen fugacity (e.g., annealing in air or Ar-atmosphere) on changes in oxidation states and potential color changes are given in Figure S1, Supporting Information.

2.2. Chemical Composition

To quantify the amount of Co in LLZO, ICP-OES measurements were performed of small parts of the single crystals. Since single crystals have no grain boundaries, it can be considered that all Co detected is incorporated in the garnet structure. In **Table 2**, the compositions of differently heat-treated samples are summarized in comparison to the intended stoichiometry of pristine LLZO, given as $Li_{6.4}Ga_{0.2}La_3Zr_2O_{12}$. The chemical compositions of the analyzed crystals reveal Co concentration of 0.002 and 0.1 Co pfu for LLZO-o and LLZO-b, respectively. Despite additional slight changes in the Ga content no significant further change has been observed. The incorporation of Co can be understood in accordance with that of Al when the LLZO green body has been placed on a corundum plate during sintering. Here, Al diffuses along the percolating Li network enabled by the relatively low activation barriers for Al[26,27] and we hypothesize that this is analogous for Co.

2.3. Structural Investigations

To understand structural changes associated with the incorporation of Co into LLZO, SCXRD on small pieces of the individual samples has been performed. Details on refinement and fitting strategies are given in Note S1, Supporting Information, and refined site occupation factors are given in Tables S1 and S2, Supporting Information. The full set of structural parameters is deposited as crystallographic information Files in the Supporting Information and under CSD numbers #2235925–2235930.

LLZO-p shows cubic symmetry, space group $I\bar{4}3d$. The superstructure, obeying $Ia\bar{3}d$ symmetry is weakly developed. As found in previous studies, Ga^{3+} orders onto the tetrahedral 12a site.[28–30] Under the assumption of similar vacancy concentrations on both tetrahedral sites, the refined Ga^{3+} content is ≈0.08 atoms per formula, this indeed is very close to the boarder of chemically induced $Ia\bar{3}d$ to $I\bar{4}3d$ symmetry change, proposed by Wagner et al.[28]

**ADVANCED
SCIENCE NEWS**

www.advancedsciencenews.com

**ADVANCED
FUNCTIONAL
MATERIALS**

www.afm-journal.de

Table 2. Chemical analysis of single crystals before and after.

		LLZO-p	LLZO-o	LLZO-b
m%	Ga	1.16(6)	1,25(2)	0,89(2)
	La	46.3(3)	41,1(3)	41,1(2)
	Li	5.24(1)	4,56(5)	4,65(7)
	Zr	21.4(4)	19,0(2)	19,1(1)
	Co	—	0013(1)	0,60(2)
	Other	29.9(7)	34,1(5)	34,2(2)
At.-ratio	Ga/Zr	0.071(2)	0086(2)	0061(1)
	Li/Zr	3.21(6)	3,15(1)	3,19(7)
	La/Zr	1.418(20)	1418(5)	1410(4)
	Co/Zr		0,0010	0048
Formula[a]		$Li_{6.34}Ga_{0.14}La_{2.84}Zr_2O_{12.4}$	$Li_{6.30}Ga_{0.17}La_{2.84}Zr_2Co_{0.0021}O_{11.7}$	$Li_{6.39}Ga_{0.12}La_{2.82}Zr_2Co_{0.096}O_{11.6}$

[a] Calculated, based on atomic ratios (using Zr = 2 pfu as fixed point). O contents are estimated from charge balance considerations.

Intensity data of pieces of LLZO-o single-crystal slabs also show SG $I\bar{4}3d$, whereby Bragg peaks obeying $Ia\bar{3}d$ symmetry, are much more intense and the $I\bar{4}3d$ superstructure is more developed compared to LLZO-p (see Figure 1c). The slight increase in electron density at the tetrahedral 12a site, while the one at 12b and 48e remains constant, suggests that Co preferentially occupies the 12a site and stabilizes in acentric symmetry $I\bar{4}3d$.

Due to slight variation in color in LLZO-b (blue vs blue greenish) two different sample batches were investigated: i) small chips of the central part of the crystal (see Figure 1b) with homogeneous deep blue color and displaying cubic symmetry $I\bar{4}3d$ (LLZO-b(c)) and ii) a sample close to the surface partly still embedded in LCO with blue greenish color to preserve the interface region (LLZO-b(s)).

Fragments of LLZO-b(c) show cubic symmetry and compared to LLZO-o the electron density at the 12a position in $I\bar{4}3d$ has increased. When modeling the increased electron density at the 12a position solely with the Li^+ scattering factor the side occupation would indicate a twice as high occupation factor value (0.52) as allowed from Wykoff site symmetry, which indicates that Co must majorly sit on this position. The minimum content of Co needed to have physical meaningful site occupation in LLZO-b crystals is 0.16 pfu, considering the 12a and 12b tetrahedral sites are fully occupied (see Table S1, Supporting Information). Some fragments of LLZO-b(s) show also cubic symmetry and behave like the LLZO-b(c) having similar high electron density at 12a, almost the same electron density at 12b and 48e sites with respect to the Li sites. The 24c (La^{3+}) and 16a (Zr^{4+}) sites appear to be fully occupied. Most other fragments of LLZO-b(s) experience a symmetry reduction from cubic $I\bar{4}3d$ to tetragonal $I4_1/acd$. This is proven by powder X-ray diffraction and evidently can be seen in direct comparison with reference pattern of cubic and tetragonal LLZO (see Figure 1d). Interestingly, among the single-crystals investigated, a decrease of tetragonal distortion with increasing Co content, expressed by the difference Δ_{tetr} between a and c lattice parameters, has been observed (see Figure 1e). While in pure end-membered $Li_7La_3Zr_2O_{12}$ Δ_{tetr} amounts 0.471 Å,[31] values between 0.07 and 0.311 Å are observed herein. All tetragonal crystals show intense twinning, nevertheless, some general information can be deduced. The structure, obtained from direct methods and residual electron density map analyses closely resembles the one found by Awaka et al.,[31] including the three clearly detectable Li positions. When refining the site occupation factors with Li only, it is evident, that systematically only the fourfold coordinated Li1 (8e) site shows overpopulation, while for the other Li sites Li2 at 16f and Li3 at 32g almost full occupation or Li deficiency is observed. The overpopulating of the tetrahedral side indicates that Co prefers in both crystal systems the same coordination sphere. Assuming a full occupation of tetrahedral 8e site in tetragonal LLZO and allowing the Li and Co content to freely adjust, a maximum of 0.13 Co pfu was identified in the bulk crystals (sizes up to 150 µm) studied (see Table S2, Supporting Information).

Further confirmation of tetrahedral coordination as well as oxidation state can be obtained by studying the characteristic absorption bands of Co via UV–vis spectroscopy (cf. Note S2 and Figure S2, Supporting Information). In Figure 1g the absorption spectra for all three samples are shown. For LLZO-p no absorption in the visible light region can be observed. For LLZO-o and LLZO-b, however, multiple absorption bands are visible. The absorption for LLZO-o takes place in the green-to-blue region, which let the crystal appear in the complementary color orange. For LLZO-b the absorption takes majorly place in the red-light region causing its blue color. The characteristic bands observed for LLZO-b can be assigned to Co^{2+} in the tetrahedral symmetry associated to three spin-allowed transitions: i) $^4A_2(F)\rightarrow ^4T_2(F)$, ii) $^4A_2(F)\rightarrow ^4T_1$ (F), and iii) $^4A_2(F)\rightarrow ^4T_1(P)$, whereby only the latter one falls in the visible region centered at about 2 eV.[23]

Further evidence is given by the HSE06 partial density of states (DOS) for cubic LLZO Co^{2+} in tetrahedral coordination as shown in Figure 1i (cf. Figures S3–S5, Supporting Information). Here, Co^{2+} introduces occupied cobalt states above oxygen states and unoccupied cobalt states in the energy gap with similar appearance compared to the absorption spectrum. Tetrahedral coordination of Co^{3+} is unfavorable coordination environment but has been observed previously for mixed-valent Co-doped YAG and YGG. Those garnets have shown a greenish color, which may be associated with the absorption in the blue (Co^{3+} on T_d) and red region (Co^{2+} on T_d) as obvious by combining

the spectra of LLZO-b and LLZO-o. The bands associated with Co^{3+} on the tetrahedral side can be potentially assigned to a $^5E \rightarrow {}^5T_2$ transition.[32] Further evidence for the assignment is again given by the partial DOS as obtained for LLZO with Co^{3+} located on the tetrahedral site having Co^{3+} unoccupied states present in the energy gap with similar appearance compared to the absorption spectrum explaining the observed orange color change.

Fourfold coordinated Co^{3+} and Co^{2+} in LLZO is in contrasts with observations made previously, where predominantly octahedral-coordinated Co^{3+} has been identified via XPS for LLZO-LCO blends annealed at temperatures between 400 and 900 °C.[22] To clarify oxidation state and local coordination of Co in LLZO, ^{57}Co Emission Mössbauer spectroscopy has been performed on samples herein, whereby only for LLZO-b, a sufficient Co signal (that is not related to Co-adsorption on LLZO) has been observed (see Figure S6, Supporting Information). The signal characteristic for Co^{3+} in octahedral coordination originates, however, from extra phases, rather than from Co incorporated in LLZO (cf. Note S3, Supporting Information). Hence, spatially resolved studies on phase-pure regions of the single crystals have been performed. Although the signal to noise ratio of the Co 2p XPS spectra is low due to the small sample size and the low Co content (cf. Note S4, Supporting Information), the chemical state of Co^{2+} was determined for LLZO-b (see Figure 1f). The asymmetric line shape of the Co $2p_{3/2}$ requires a main component (A) and satellite (B), whose binding energy shift is characteristic for Co^{2+},[33] which further supports the findings made by SCXRD and UV–vis spectroscopy.

As outlined above, the total Co content in tetragonal LLZO scales with the tetrahedral deviation Δ_{tetr} from cubic symmetry. Astonishingly, the two crystals with largest Δ_{tetr} values (extracted close to the LCO|LLZO interface) showed almost no Co incorporation (see Figure 1e and Table S2, Supporting Information). After full refinement with anisotropic atomic displacement parameters for the framework atoms (La, Zr, and O) and isotropic refinement of the Li1, Li2, and Li3 positions, a remaining residual electron density is found in all tetragonal samples, except those with very low Co contents. The residual is located at a position of $\approx 0.38, 0, ¼$, which is very close to the Li1 12a position in cubic $I\bar{4}3d$ at $^3/_8, 0,$ and ¼. This position is in between the Li2 (16f) and Li3 (32g) position of tetragonal crystals and may be seen as a kind of positional disorder in due course of beginning transformation to cubic symmetry. As mentioned, the anisotropic distortion of LLZO toward a tetragonal phase, when the Co decreases, contrasts with our expectations. Based on our findings, we hypothesize that the Co incorporation in LLZO leads to Ga dissolution (although both have the same oxidation state and similar ionic radii) and lattice distortion that introduces high residual stresses due to lattice constraints toward the bulk. The build-up of elastic energy gets finally released by fracture. Since Co is not thermodynamically stable in LLZO structure, we believe that Co will segregate at the fracture surfaces by stress-mediated diffusion.[34] Since the Ga originally present to stabilize the cubic phase has been removed in favor of Co, LLZO undergoes a phase change to tetragonal LLZO. Moreover, the fracture of the LLZO crystal leads to a slight tilting between the new formed LLZO domains explaining the complex twinning behavior observed.

At the LCO|LLZO interface region of LLZO-b(s) a thin decomposition zone is observed. Due to prolonged exposure and high temperature, this zone is well developed and consists mainly of Li_2CO_3, blue-black CoO (see black spots in Figure 1b), and small amounts of a dark brownish phase. No indications of $La_2Zr_2O_7$ or $LaCoO_3$ as reported by Varda et al.[18] were found by PXRD (see Figure S7, Supporting Information). A single-crystal of the brown phase, around 60 μm in size, was extracted and examined by single-crystal X-ray diffraction. This phase is cubic, space group $Im\bar{3}m$, with refined composition $LaLi_{0.95}Co_{0.26}O_{2.0}$, like an iron containing compound reported by Mazza et al.[35] containing octahedral coordinated Co^{3+}. This further supports investigations made by Vardar et al.[18] that La–Co–O decomposition phases with varying stoichiometry are formed at the LLZO|LCO interface. No crystalline Zr-containing decomposition phase is observed, supporting the assumption that Zr is rigidly bonded in LLZO and is not majorly taking part in inter-diffusion processes.

2.4. The Impact of Co on the Band Structure and Electrochemical Stability

A colorization of LLZO can be linked to a narrowing of the optical band gap, with potential implications on the electrochemical stability window.[36] Therefore, we determined the optical band gap via UV–vis spectroscopy and performed CV experiments to correlate the bandgap to potential changes in the electrochemical stability.

To estimate the band gap we plotted the absorption spectra (see Figure 1g) in a Tauc plot fashion $((Ah\nu)^2$ vs h$\nu)$, with A being the absorption coefficient and $h\nu$ describing the energy of light at a certain measured wavelength λ, which allows the direct read out of the optical band gap at the intercept of the first slope of the linear part of the Tauc plot with the x-axis (see Figure 1h). The band gap for LLZO-p is 4.78 eV and in good agreement with values reported previously.[37] The band gap significantly narrows in dependence of the amount of Co incorporated. For LLZO-o and LLZO-b, the optical band gap is as low as 2.6 and 1.6 eV, respectively.

The electrochemical stability window has been determined via cyclic voltammetry (see **Figure 2**a). To increase the sensitivity of the experiment by increasing the active surface area of LLZO we produced a slurry consisting of ball milled LLZO samples (cf. Experimental Section). For LLZO-p and LLZO-o no significant faradaic reactions could be measured (see Figure 2a). Interestingly, for LLZO-b, an oxidative reaction could be observed at about 4.0 V. To check if this process is reversible, we cycled the cell in a voltage range of −1.0 to 4.5 V. However, no indication of a corresponding reduction peak occurred. In subsequent cycles, neither oxidation nor reduction peaks could be observed, indicating a kinetically induced stability.[38] We hypothesize, that the oxidation of Co^{2+} to Co^{3+} leads to a destabilization of the LLZO structure (due to high Co concentration), hence, to a decomposition of LLZO, probably forming a stable interphase. Alternatively, this could also be related to the decomposition of the found extra phase $LaLi_{0.95}Co_{0.26}O_{2.0}$. Further studies are, however, needed to evaluate our assumptions.
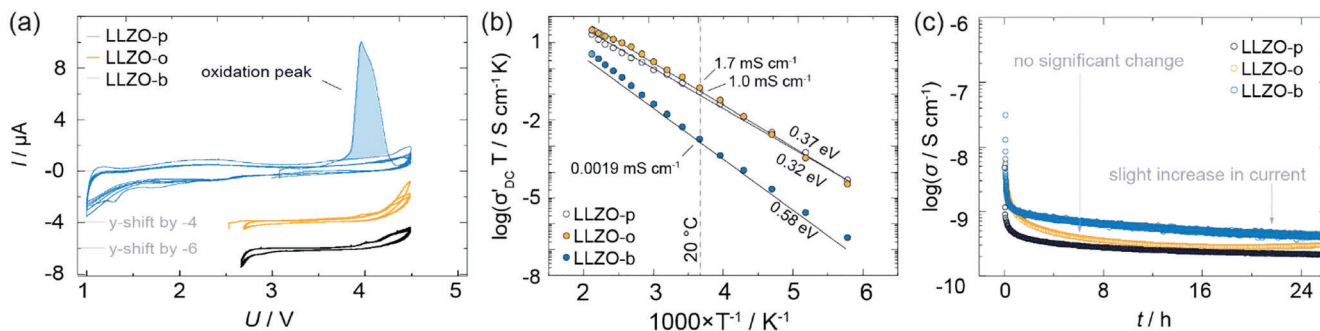
Figure 2. a) First three cycles of cyclic voltammetry measurements of Li|LLZO-p|Au (black), Li|LLZO-o|Au (orange), and Li|LLZO-b|Au (blue) half cells in a range of 2.5 to 4.5 and 1.0 to 4.5 V, respectively. LLZO-b shows an oxidation peak at ≈4.0 V in the first cycle. b) Arrhenius plot of corresponding samples. While LLZO-o shows a slight increase in Li-ion conductivity compared to LLZO-p, the ionic conductivity in LLZO-b decreased by >3 orders of magnitude at room temperature. c) DC polarization measurements of corresponding samples. Electronic conductivity only increases slightly for LLZO-b.

2.5. The Impact of Co on the Electrical Conductivity

To understand the impact of Co doping on the ionic and electronic conductivity as well as its thermal activation, we performed electrochemical impedance spectroscopy (EIS) and DC polarization experiments.

The DC ionic conductivity σ_{DC} of all samples between −60 to 180 °C was determined from the frequency independent DC plateaus in the bode plot (cf. Note S6 and Figure S8, Supporting Information). For LLZO-p, a room temperature bulk ion conductivity of $\sigma_{bulk,RT} = 1.1$ mS cm^{-1} could be determined. For LLZO-o the conductivity even slightly increased to $\sigma_{bulk,RT} = 1.2$ mS cm^{-1}. The increase in Li-ion conductivity may result from the increasing number of dopants on the Li-sites (Ga + Co) associated with, for example, changes in structure, phase, and defects concentration.[39] A further increase in the Co concentration leads, however, to significant drops by >3 orders of magnitude to an ionic conductivity $\sigma_{bulk,RT} = 7.60 \times 10^{-7}$ S cm^{-1} as observed in LLZO-b. This reduction could be related to a lowering in symmetry to the tetragonal garnet phase in certain regions of the crystal, which is in agreement with the values reported for this phase previously.[40]

All samples follow Arrhenius-type behavior in accordance with $\sigma_{DC} = A \exp(-E_a/k_B T)$, with A denoting the pre-exponential factor of the ionic conductivity σ_{DC}, E_a being the activation energy, the Boltzmann's constant and absolute temperature are given by k_B and T, respectively. LLZO-p and LLZO-o exhibit comparable activation energies of 0.30 and 0.34 eV. For LLZO-b a significant increase in the activation energy $E_a = 0.54$ eV was observed (see Figure 2b). In order to differentiate between Li-ion and electron conductivity, we performed DC polarization experiments on LLZO-p, LLZO-o, and LLZO-b (see Figure 2c). The electron conductivity σ_{eon} was calculated from the polarization current I by $\sigma_e = I/U_{pol} \times h/A$, where U_{pol} denotes the polarization potential with $U_{pol} = 100$ mV, and h and A being the thickness and the area of the samples. For LLZO-p, we calculated an electron conductivity of $\approx\sigma_e = 2 \times 10^{-10}$ S cm^{-1}, which is in accordance with values reported by Philipp et al.[41] No significant changes have been observed for LLZO containing Co, that is, LLZO-o and LLZO-b ($\sigma_e \approx 4 \times 10^{-10}$ S cm^{-1}). Interestingly, the ionic conductivity σ, the activation energy E_a, and the electron conductivity σ_e, respec-
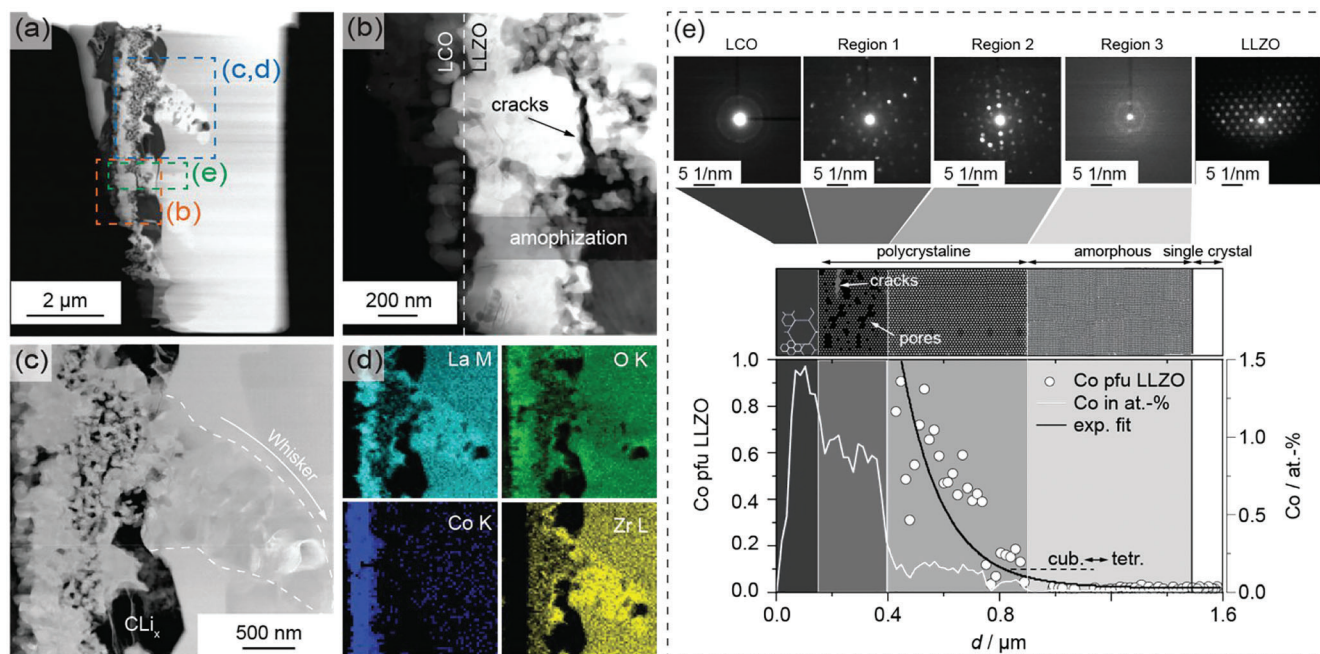
tively, exhibited by LLZO-b and values published in literature for tetragonal LLZO are in a good agreement.[31,42]

2.6. Interfacial Degradation

To understand the Co-incorporation mediated degradation processes taking place at the LLZO|LCO interface, cross-sectional imaging of annealed LCO-sputtered LLZO was performed using scanning transmission electron microscopy (STEM) and high-angle annular dark-field (HAADF) imaging (see **Figure 3**a–c). The LCO layer could clearly be discerned showing a thickness of ≈150 nm and exhibiting a nano crystalline morphology with lateral crystallite sizes in the range of 30–100 nm (see Figure 3b). Measurements revealed a high degree of distortion of the LLZO crystal close to the LLZO|LCO interface within a depth of ≈1.3 µm from the surface, with polycrystalline whiskers reaching even deeper depths. One of these whiskers is highlighted in Figure 3c with corresponding elemental energy-dispersive X-ray spectrometry (EDX) analysis shown in Figure 3d revealing an increased Zr and La content and a decreased O content within the whisker. Most likely these phases can be assigned to LaLi$_{0.95}$Co$_{0.26}$O$_{2.0}$ and La-deficient tetragonal LLZO as revealed by SCXRD. In general, this region is governed by a rather polycrystalline, yet porous structure with several extended voids (see Figure 3c,e). These pores seem to be filled with a carbon containing species as revealed by electron energy loss spectrometry (EELS) analysis (cf. Figure S9, Supporting Information), which could be assigned to Li$_x$C.

EDX and EELS (see Figure 3d; cf. Figure S7, Supporting Information) data, furthermore, allows distinguishing between a Co rich phase (region 1, 250 nm) and a phase with a lower Co content (region 2, 500 nm) as indicated in Figure 3e. Both phases are characterized by a similar amount of La, which is lower compared to the pristine region. Further, in depth nano-beam electron diffraction (NBED) measurements (see Figure 3e; cf. Video S1, Supporting Information) confirm the polycrystalline nature of the regions and disclosed another intermediate phase (region 3, 650 nm), which is mostly amorphous without a significantly different composition compared to the adjacent single-crystalline LLZO region. Despite the confirmation of the cubic garnet

**ADVANCED
SCIENCE NEWS**

www.advancedsciencenews.com

**ADVANCED
FUNCTIONAL
MATERIALS**

www.afm-journal.de

Figure 3. Cross-sectional STEM analysis of a representative LCO|LLZO interface region of sample LLZO-b after annealing. a) Overview HAADF image showing the TEM lamella. The denoted regions are magnified and depicted in (b–e). b) Magnified region of (a) highlighting microstructural degradation processes, such as fracture and amorphization. c) ADF micrograph highlighting the polycrystalline nature of the depicted region. d) EDX maps of La, Co, O, and Zr of the region containing a polycrystalline whisker. e) NBED results obtained from different positions within the sample cross-section. The inset in the overview HAADF micrograph shows the EELS signal for Co, obtained from a line-scan over the same sample region.

structure of the single crystal in the pristine regions as well as its [110] crystallographic orientation a precise assessment of the degradation products has been hindered by the limited angular resolution of the technique and the high number of possible structures and crystallographic orientations of the involved oxides.

It is interesting that the amorphization of LLZO enhances toward the bulk before approaching the single crystalline region (see Figure 3e). We propose that small amounts of Co (<0.1 Co pfu) can already build up residual stresses high enough to cause the fracture in LLZO. The fracture in LLZO leads to an increased surface area promoting Co cross diffusion, hence, fostering the degradation of LLZO (formation of extra phases). The phases formed may crystallize and result in grain growth at given temperatures (large single crystals of extra phases have been found herein supporting this hypothesis, see section 2.3), which could explain the more crystalline nature of these regions (i.e., sharper Bragg peaks) and lower sintering temperature of the newly formed phases. This could also explain whisker-like structures considering that crack expansion could promote locally extended degradation processes.

2.7. Process Diagram and Mitigation Strategy

Knowing the temperature dependency of Co, as well as the approximate Co concentration that led to detrimental effects on performance we can simulate the impact of different processing parameters, such as temperature and time, on the diffusion profile, hence, the temperature that will lead to high interfacial

impedances. In order to determine the diffusion coefficient of Co we analyzed the diffusion profiles of LCO-sputtered LLZO annealed in air at temperatures between 600 to 700 °C via STEM and TOF-SIMS as shown in Figures S9 and S10, Supporting Information, respectively (cf. Note S6, Supporting Information). The Diffusion coefficient for a given temperature can be obtained by the following equation.
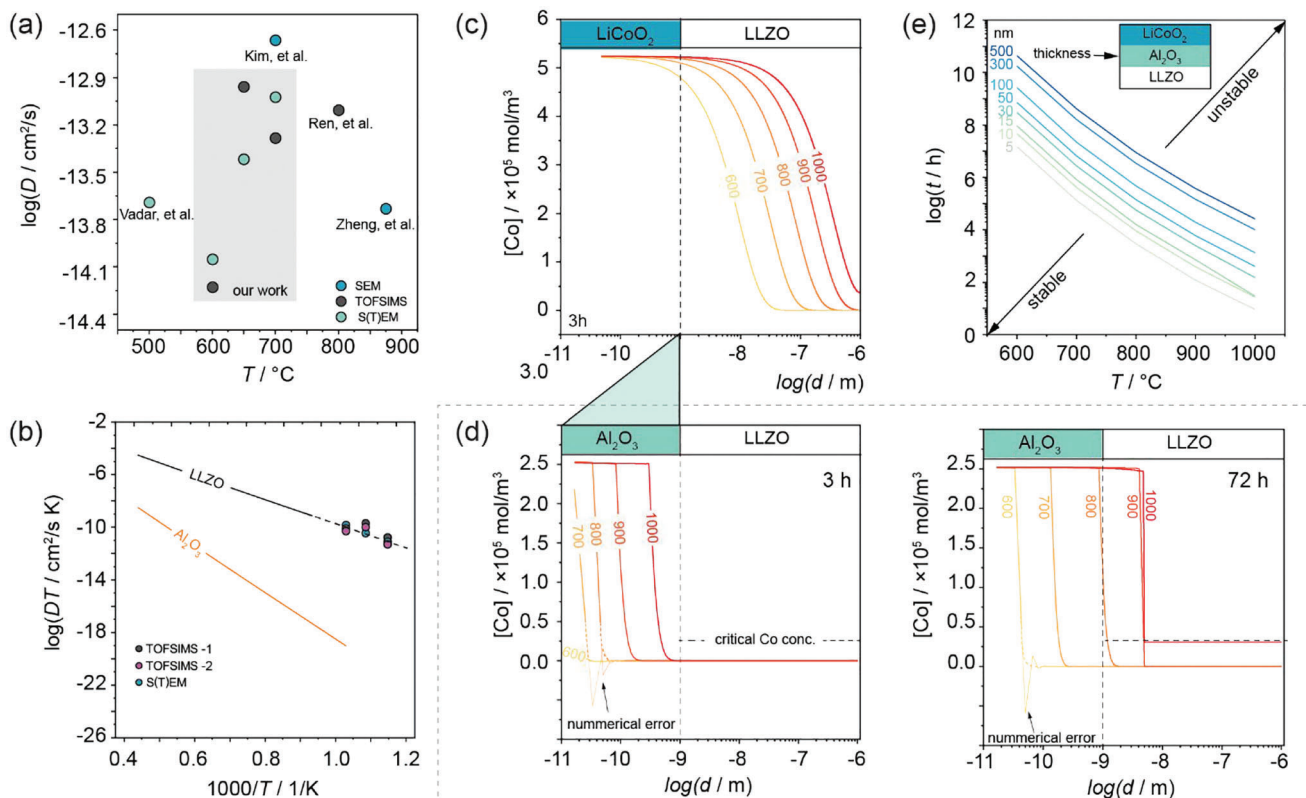
$$y = \frac{c1 + c2}{2} \times \left[1 - \mathrm{erf}\left(\frac{x}{2\sqrt{Dt}} \right) \right] \qquad (1)$$

where c_1 and c_2 represent the Co concentrations in LCO and LLZO, D is diffusion constant, and t represents the total time for which Co diffusion takes place at a particular temperature. The Diffusion coefficients for the individual temperatures are plotted in **Figure 4**a comparing with values from literature. Significant variations can be observed, even for similar temperatures. For example, these variations can be associated with microstructure[43,44] (i.e., we used single crystals without grain boundaries) or the oxygen fugacity (e.g., annealed in air or in Ar; cf. Figure S1, Supporting Information).

To estimate the diffusion profile for any given temperature the Arrhenius equation

$$D(T) = D_o \exp(- E_a / RT) \mathrm{m}^2 \mathrm{s}^{-1} \qquad (2)$$

has been utilized by plotting the diffusion coefficients in an Arrhenius fashion (Figure 4b). Where, D is the diffusion coefficient (in $\mathrm{m}^2 \mathrm{s}^{-1}$), D_0 is the maximal diffusion coefficient (at infinite temperature; in $\mathrm{m}^2 \mathrm{s}^{-1}$), E_a is the activation energy for

ADVANCED
SCIENCE NEWS
www.advancedsciencenews.com

ADVANCED
FUNCTIONAL
MATERIALS
www.afm-journal.de

Figure 4. a) Diffusion coefficient of Co in LLZO samples evaluated in this work and reported literature. b) Arrhenius plot showing the change in Co diffusion coefficient with increasing temperature. The dashed line with symbols represents the experimental data and the continuous lines depict the simulated data. c) Predicated Co diffusion of Co in LLZO for various sintering temperatures and fixed sintering time of 3 h through finite element analysis. d) Predicated diffusion of Co in LLZO with 10 nm thick Al_2O_3 layer at various sintering temperatures and fixed sintering time of 3 and 72 h revealing that longer sintering time has least impact on Co diffusion through LLZO at temperatures below 1000 °C. e) The predicated temperature dependent Co diffusion in LLZO with various Al_2O_3 interlayer thicknesses with time till a critical Co concentration is reached, which results in phase transition in LLZO from cubic to tetragonal and leads to reduction in Li ion conductivity of LLZO by two orders of magnitudes.

diffusion (in kJ mol⁻¹), T is the absolute temperature (in K) and $R \approx 0.00831$ kJ mol⁻¹ K⁻¹ is the universal gas constant.

In Figure 4c the diffusion profiles for an annealing time of 3 h from 600 to 1000 °C are shown. It is apparent that the temperature affects the diffusion length. An increase from 600 to 1000 °C leads to an increase by a factor of 100. In contrast a change in the dwelling time has no significant effect on the diffusion profile, considering typical processing conditions (see Figure 4e). Based on the diffusion profile the Co concentration will significantly exceed the solubility limit of Co in LLZO at any relevant temperature causing structural degradation and evolution of extra phases. Hence, the decomposition of LLZO at the interface is unavoidable, but might not be as detrimental for temperatures below 500 °C due to a relatively thin decomposition zone of about 10 nm, which may introduce only slight impedance changes. Considering previous reports on temperature requirements to form a good intermediate conduct to achieve sufficient performance, temperatures above 800 °C are required. A strategy proposed by Ren et al.[45] to overcome this challenge is to introduce a protective layer, Al_2O_3, to avoid the incorporation of Co. The authors reported that the role of Al_2O_3 coating is to lower the interfacial energy by Al dif-

fusion into LCO, thereby preventing the reaction between LCO and polycrystalline LLZO and hindering the Co cross diffusion. Other studies have shown that the incorporation of Al in LCO could result in the formation of a spinel phase $LiAl_xCo_{1-x}O_2$[46] whilst Co diffusion into Al_2O_3 is associated with the formation of $CoAl_2O_4$ spinel and the corresponding temperature dependent diffusion coefficients have been reported.[47] The authors claimed that the Co diffusion in Al_2O_3 is limited by the sintering temperature. At lower temperatures the spinal phase is formed leading to lower Co diffusion coefficient and vice-versa. The Co diffusion coefficient for both Al_2O_3 and $CoAl_2O_4$ phases is rather similar, and the Co will first be used to form the spinel phase when a certain Co concentration is reached, which will at least slow down the build-up of a critical Co concentration. In respect of the desired performance of the SSB the resistive passivation layer must be kept at a minimum to minimize any contribution to interfacial resistance. In our model we introduced an Al_2O_3 layer with the boundary condition that when a certain Co concentration is reached (i.e., spinel phase is formed) it stays constant. In Figure 4d diffusion profiles for a fixed Al_2O_3 thickness of 10 nm is shown. It can be seen that for a given temperature up to 1000 °C hold for 3 h no cross-diffusion takes place indicating that Al_2O_3 can protect LLZO from degradation. Increasing the

**ADVANCED
SCIENCE NEWS**

www.advancedsciencenews.com

**ADVANCED
FUNCTIONAL
MATERIALS**

www.afm-journal.de

holding time to an extended duration, we can observe that at temperatures above 800 °C, degradation takes place, whereby the interphase formation remains in the sub-nm range. Moreover, Figure 4e illustrates the role of coating thickness to protect LLZO from degradation. It allows to select appropriate coating thickness without large compromise in respect of interfacial transport kinetics. For example, having Al_2O_3 coating of only 5 nm allows to anneal LLZO with LCO at 1000 °C for almost 10 h without expecting degradation.

3. Conclusion

In this study, the role of Co on degradation processes taking place at the LLZO|LCO interface during annealing is presented. First, we investigated the incorporation of Co into LLZO during high temperature treatment and analyzed its consequences on structure, microstructure, and electrochemical performance. We found, depending on the oxygen fugacity, Co^{2+} and/or Co^{3+} incorporates into the LLZO lattice occupying tetrahedral positions. Depending on oxidation state color changes from transparent, orange, and blueish are observed. When low amounts of Co incorporate into LLZO a more ordered acentric cubic phase is observed, accompanied by a slight increase of the Li-ion conductivity up to 1.3 mS cm^{-1}. When a Co content exceeds a critical value at around 0.16 pfu a phase transition to the low conductive tetragonal LLZO modification is observed, which is associated with a decrease in Li-ion conductivity by three orders of magnitude. Although, introducing 3d-electronic states into LLZO, no change in the electronic conductivity is observed. The structural changes seem to be associated with high stresses causing fracturing of LLZO until complete amorphization is reached. Due to the increased surface area the leaching of La, Li, and Co from LLZO and LCO to form $LaLi_{0.95}Co_{0.26}O_{2.0}$ is accelerated promoting degradation into the materials interior. The incorporation of Co into LLZO for the formed extra phases leads to an oxidative instability when cycled to high potentials. This process is irreversible but kinetically self-limiting.

Thereafter, we measured the Co diffusion coefficient for a wide temperature range to determine the corresponding time for a given temperature until a critical Co concentration is reached. This temperature-depended diffusion coefficient is determined and shows that cross-diffusion into LLZO and the associated degradation of LLZO is unavoidable for relevant processing conditions. To mitigate cross-diffusion the introduction of a protecting layer Al_2O_3 has been studied. Based on FEA studies we propose a process diagram that allows to select processing conditions, that is, coating thickness, temperature, and time to enable the efficient interface engineered cell design without degradation and a minimum compromise in electrochemical performance, which is key to enable high energy density SSBs.

4. Experimental Section

Synthesis: Single crystalline $Li_{6.4}Ga_{0.2}La_3Zr_2O_{12}$ garnets were synthesized out of a melt using the Czochralski method. This method was chosen as it yields in large crystals with homogeneous elemental distribution compared to polycrystalline samples. For the synthesis, stoichiometric amounts of Li_2CO_3 (Alfa Aesar, 99.999%), La_2O_3 (Fox Chemicals, 99.999%), and ZrO_2 (Merck, Optipur) and Ga_2O_3 (Fox Chemicals,

99.999%) were mixed. Due to Li evaporation during the sintering step, an excess of 10% Li_2CO_3 was added. For the preparation of the single crystals, the as-prepared polycrystalline LLZO samples were inductively heated and melted in an Ir crucible under N_2 atmosphere. After supercooling the melt, an Ir wire was dipped into the crucible to induce crystal growth. This wire was then pulled out of the melt with a constant rate of 0.4 mm h^{-1} for 15 h with a rotation of 10 rpm until the melt was cooled down to room temperature. This resulted in a yellowish single crystal, which was transparent from the inside and had a size of $\approx\varnothing = 14$ mm and $h = 50$ mm. For further experiments, the crystal was cut into pieces.

To incorporate different amounts of Co, a LLZO single crystal was placed in a Cu tube and the tube was filled with LCO powder to completely cover the LLZO single crystal with LCO. The tube was then sealed under vacuum before it was heat treated at different temperatures and dwelling times under Ar to avoid Cu oxidation. After the heat treatment, the embedded single crystals were covered in a solid coating being surrounded by a metallic-appearing surface, which was removed by sanding. After removing the LCO coating, single crystals were obtained with colors ranging from almost transparent to blue depending on the treatment history. For simulating degradational effects on the LCO-LLZO interface, two experiments were conducted: First, 100 nm of LCO was magnetron sputtered onto one side of different LLZO single crystals acting as a thin film cathode. Each of these crystals were tempered at various temperatures between 600–700 °C for 48 h under air atmosphere to simulate different annealing times resulting in orange-colored crystals. In the second preparation method, the aim was to simulate an extreme case of Co cross diffusion. Therefore, transparent, single crystalline LLZO ($A \approx 12$ mm^2, $h \approx 0.5$–1.0 mm) and LCO powder were placed inside a Cu tube. After densifying the powder to guarantee a good LCO|LLZO contact, the Cu tube was sealed on both sides and tempered at 500 and 900 °C for 5 days under Ar flow in a ceramic tube oven. After heating, the remaining LCO powder was removed and the LCO incorporated LLZO crystals were polished with a sand-paper with 4000 grit. This extreme case will further be referred to as route 2. If not stated elsewhere, both route 1 and route 2 were used for all sample preparations.

ICP-OES: ICP-OES analysis was performed using an iCAP 6500 RAD (Thermo Fisher Scientific, USA). For data acquisition, Qtegra software provided by the manufacturer was used. Sample digestion was performed using a borax fusion: 5–10 mg sample were mixed with 0.5 g borax and heated to 1000 °C for 5 h. The solidified fusions were dissolved at 70 °C using an HCl/HF/H$_2$O mixture (10 m% HCl, 0.8 m% HF). A univariate calibration using certified single element ICP-standard solutions was used for signal quantification. For the correction of instrumental drifts and variations in sample introduction, Eu was added to all measured solutions and used as internal standard. More detailed information on the procedure used for the bulk analysis of LLZO via ICP-OES can be found elsewhere.[35]

Single-Crystal X-Ray Diffraction: Single-crystal X-ray diffraction data were collected on a Bruker SMART APEX CCD-diffractometer. The single crystals, selected on the basis of their optical properties (regular shape and homogeneity in color) were glued on top of glass capillaries (0.1 mm $\varnothing$). Intensity data were collected with graphite-monochromatized Mo K$_\alpha$ X-radiation (50 kV, 30 mA); the crystal-to-detector distance was 30 mm and the detector positioned at $-30°$ and $-50°$ 2Θ using an ω-scan mode strategy at four different ϕ positions (0°, 90°, 180°, and 270°) for each 2Θ position. 630 frames with $\Delta\omega = 0.3°$ were acquired for each run. With this strategy, data in a large Q-range up to minimum d_{hkl}-values $d = 0.53$ Å could be acquired. This was necessary for accurate determination of anisotropic displacement parameters and to reduce correlation effects between atomic displacement parameters and site occupation numbers. 3D data were integrated and corrected for Lorentz-, polarization and background effects using the APEX4 software.[48] Structure solution (using direct methods) and subsequent weighted full-matrix least-squares refinements on F^2 were done with SHELX-2012, [49] as implemented in the program suite WinGX 2014.[50]

^{57}Co Emission Mössbauer Spectroscopy: For the Mössbauer experiments, about 25 MBq ^{57}Co as an aqueous solution of $Co(NO_3)_2\cdot6H_2O$ was added to each LLZO-p and LLZO-b. Both samples were then dried in air at 120 °C for 6 h after the ^{57}Co probing procedure. ^{57}Co Mössbauer

ADVANCED
SCIENCE NEWS

www.advancedsciencenews.com

ADVANCED
FUNCTIONAL
MATERIALS

www.afm-journal.de

emission spectra were collected at room temperature with a constant-acceleration spectrometer using a $K_2MgFe(CN)_6$ absorber. Velocity calibration was carried out using sodium nitroprusside at room temperature and isomer shifts were given relative to metallic iron. The [57]Co Mössbauer spectra were fitted using the Mosswinn 4.0 program.

X-Ray Photoelectron Spectroscopy: The experiments were performed in an ultrahigh vacuum (UHV) chamber (pressure $<5 \times 10^{-10}$ mbar) at room temperature (RT). XPS core level spectra were obtained using the Mg Kα (1253.6 eV) and Al Kα (1486.6 eV) lines and a Phoibos 150 electron analyzer with the axis coincident with the surface normal. The core level binding energies were calibrated using the binding energies of C 1s and Ag 3d in contact with the sample as references.

A Shirley background and asymmetric singlet pseudo-Voigt functions were used for data analysis and core level peak fitting. The fit was optimized using a Levenberg–Marquardt algorithm with a routine running in IGOR Pro (WaveMatrix Inc.).[51] The quality of the fit was assessed by a reliability factor, the normalized χ^2.

The samples were measured as introduced and after mild annealing in UHV to remove surface hydroxylation. The small size of the samples and the low Co content had limited the signal to noise ratio of the data obtained for Co. However, relevant information about the Co oxidation state could be extracted.

Optical Absorption Spectroscopy: For the optical absorption measurements, the absorption A of differently LCO treated LLZO samples was investigated. The measurements were conducted using a UV–vis spectrometer equipped with optical fibers and a 1024-pixel diode-array detector (J&M Analytik AG, Essingen, Germany) in a range of 200 to 1000 nm while the sampling time was set to 2 min. The samples were abraded until a thickness of $h \approx 0.8$ mm and pre-polished with a ZrO_2 sandpaper (4000 grit).

Computation Methods: First-principles calculations were performed with the Vienna ab initio simulation package[52–54] to predict the DOS of Co-doped LLZO. Core-valence electron interactions were treated with the projector-augmented wave method.[55] The semi-local generalized gradient approximation of Perdew–Burke–Ernzerhof[56] was used for ionic relaxations and the Heyd–Scuseria–Ernzerhof of hybrid functional (HSE06) with a screening parameter of 0.11 bohr^{-1} was used for DOS calculations.[57,58] The electronic convergence was set to 10^{-4} eV and an energy cutoff of 400 eV was used. All atom positions were relaxed until the forces were less than 0.05 eV Å^{-1}. Spin polarized electronic occupancies were determined using Gaussian smearing with an energy-broadening of 0.1 eV and a Gamma-only k-point mesh.

The experimental Li56La24Zr16O96 crystal structures adopted for these calculations were the acentric cubic (I-43d), cubic (Ia-3d), and tetragonal (I4$_1$/acd). For the cubic modifications, disordered lithium distributions were selected to satisfy experimental occupancies and to avoid unfavorable nearest-neighbor occupations. The resulting Li occupancies in the I-43d space group for the 12a/12b and 48e sites were 1.0 and 0.667, respectively; for the Ia-3d space group, the 24d and 96h site occupancies were 0.542 and 0.448, respectively. Cobalt was positioned on the 12a and 48e lithium sites in the I-43d structure, on the 24d/96h sites in Ia-3d, and on 8a and 16f sites in I4$_1$/acd. The lithium concentration in the simulation cell was adjusted to accommodate the Co^{2+} and Co^{3+} oxidation states.

Electrochemical Impedance Spectroscopy: In order to study the influence of Co content in LLZO on electrochemical properties and long-range Li ion diffusion, EIS measurements were performed. Samples with thickness of $h \approx 0.5–1.0$ mm and an area $A \approx 12$ mm^2 were used. Au blocking electrodes were applied on both sides of the crystals with a thickness of 100 nm using a LEICA EM SCD 050 sputter device. For measuring the impedance between 10 mHz to 1 MHz, a Novocontrol Concept 80 broadband dielectric spectrometer was used while a root-mean-square (rms) sinusoidal voltage amplitude of 100 mV rms was applied. The temperature in the BDS 1200 sample cell was controlled using a QUATRO cryosystem while the samples were measured under a steady N$_2$ stream between −60 and 180 °C in 20 °C steps.

For the determination of the electronic conductivity of the samples, which were previously measured with EIS, direct current (DC) polarization measurements were conducted on a Parstat MC potentiostat with low current option. A constant potential of 100 mV was applied while a memmert

UN30 heating oven guaranteed a steady temperature of 20 °C during the measurements.

Cyclic Voltammetry: To investigate the redox activity of Co incorporated LLZO, cyclic voltammetry was conducted between 1.0 to 4.5 V using a Biologic MPG-03. The scan rate was set to 25 µV s^{-1}. For the preparation of the cathode electrodes, Co incorporated LLZO crystals were pre-ground using a mortar and a pestle. Conductive carbon (Super C65) (4 wt%) and binder (Kynar Flex 2801) (6 wt%) were added to ground LLZO (90 wt%). For a better homogenization during the following milling step, the mixture was dissolved in *N*-methyl-pyrrolidone. After milling at 400 rpm for 40 min, the slurry was tape-casted onto a pre-etched Al foil with a thickness of 100 µm. Subsequently, the cast was pre-dried overnight at 60 °C in a heat drying oven. Afterward, electrode discs with a diameter of 3 mm were punched out of the cast and dried at 60 °C in a vacuum oven (Büchi) overnight again. Resulting cathodes were transferred into an Ar-filled glovebox, in which the whole cell assembly was conducted. For the measurements, Swagelok T-cells in a two-electrode setup were used, whereas Li (Ø = 3 mm; Aldrich) served as the anode. To avoid direct contact and thus, prevent the cell from an internal short circuit, metallic Li was shielded from the cathode electrode by a semipermeable glass fiber separator (Whatman glass microfiber filters GF/F). To guarantee good Li ion transport during the measurement, 1 M LiPF$_6$ in a mixture of ethylene carbonate:dimethyl carbonate in a ratio of 1:1 acted as the liquid electrolyte.

Scanning Transmission Electron Microscopy Characterization: Samples for the STEM experiments were extracted from the bulk with a focused (Ga-) ion beam SEM Dual Beam microscope (FEI NOVA 200), following a standard procedure. The lift out and initial milling step was done with 30 kV ions and the final milling step was performed at 5 kV. The extracted lamellae were mounted onto an Omniprobe copper-based lift-out grid and directly transferred to the microscope. STEM observations were carried out by a probe corrected FEI TITAN3 G2 microscope operated at 300 kV. The microscope was equipped with a highly sensitive four-quadrant SSD detector for EDX and a Gatan GIF Quantum for EELS measurements. The convergence angle was set to 19.6 mrad for standard imaging and spectroscopy while for NBED this angle was reduced to 0.45 mrad. Data acquisition and analysis was performed with the Gatan Microscopy Suite (GMS, version 3.4.). The NBED data was analyzed with CrysTBox v 2.21.

TOF-SIMS: In order to investigate cross diffusion phenomena in LLZO, samples were prepared by sputtering LCO thin films (105 nm) onto LLZO single crystals at room temperature. The samples were then annealed at 600, 650, and 700 °C for 24 h under air. Subsequent TOF-SIMS depth profiling was performed at room temperature. Diffusion profile measurements were performed on a TOF.SIMS 5 (ION-TOF, Germany) instrument. 25 keV Bi$^+$ primary ions were used in spectrometry mode. Areas of 100×100 µm^2 were investigated using a raster of 256×256 measured points. Positive secondary ions and clusters were analyzed up to mass 164 u, and the intensities of all relevant secondary ions and clusters were analyzed simultaneously. Depth-profiling was performed with 2 keV O^{2+} ions (400×400 µm^2, ≈850 nA) via sequential ablation of the surface between measuring secondary ions in non-interlaced mode. A low energy electron flood gun (21 eV) was used for charge compensation. After TOF-SIMS analysis, the depth of the sputter craters was measured with a stylus profilometer (DekTakXT, Bruker, USA) to convert sputter time into depth.

Finite Element Analysis: The diffusion of Co into the alumina and LLZO layers and the formation of the spinel phase were modeled using COMSOL software with following assumptions. The modeling focused on Co diffusion in the Al$_2$O$_3$ and LLZO layers. LCO was assumed as the source of cobalt and its concentration was presumed to be constant and equal to the concentration in its structure.

Spinel Simulation: The Co diffusion in Al$_2$O$_3$ layer resulted in the formation of spinel phase (CoAlO$_3$). The concentration of the cobalt inside the structure cannot exceed the maximum capacity of the Al$_2$O$_3$ (0.0252 mol of Co cm^{-3}).

Boundary Conditions: The concentration in the X direction which is perpendicular to the LCO interface was of interest. Therefore, the "symmetry" boundary conditions were used for top and bottom boundaries. The cobalt concentration at the LCO│Al$_2$O$_3$ interface (left-side boundary) was assumed 0.0524 mol cm^{-3}, which is the cobalt concentration that can be

provided by the LCO to the neighboring layer. No-flux boundary condition (concentration gradient equal to zero) was considered for LLZO's right face (right-side boundary).

Initial Conditions: The Co concentration was initially zero in both Al_2O_3 and LLZO layers.

Transport Equation: The transport of the Co ions through the solid layers was governed by Fick's second law. Each layer had its own diffusion coefficient.

Diffusion Coefficients: The diffusion coefficient of Co and its temperature dependency in Al_2O_3 layers was estimated using diffusion equation as reported by Moya et al.[47] For the LLZO layer, the equation of the linearly regressed line passed through this experimental data was hired to calculate the diffusion coefficients at different temperatures.

Mesh: The meshes were refined in the X direction in the Al_2O_3 layer and close to the $Al_2O_3 \mid$ LLZO interface. The number of elements in the X direction in Al_2O_3 and LLZO layers was 300 and 2300, respectively. Thickness of the Al_2O_3 and LLZO layers were assumed 5 nm and 1 µm respectively. The modeling of the diffusion with different Al_2O_3 thicknesses and without Al_2O_3 was also reported, however, the LLZO thickness (1 µm) was kept constant.

Supporting Information

Supporting Information is available from the Wiley Online Library or from the author.

Acknowledgements

Conflict of Interest

The authors declare no conflict of interest.

Data Availability Statement

The data that support the findings of this study are available from the corresponding author upon reasonable request.

Keywords

[1] V. Thangadurai, W. Weppner, *J. Am. Ceram. Soc.* **2005**, *88*, 411.
[2] V. Thangadurai, H. Kaack, W. Weppner, *J. Am. Ceram. Soc.* **2003**, *86*, 437.
[3] R. Murugan, V. Thangadurai, W. Weppner, *Angew. Chem., Int. Ed.* **2007**, *46*, 7778.
[4] A. Banerjee, X. Wang, C. Fang, E. A. Wu, Y. S. Meng, *Chem. Rev.* **2020**, *120*, 6878.
[5] K. V. Kravchyk, D. T. Karabay, M. V. Kovalenko, *Sci. Rep.* **2022**, *12*, 1177.
[6] M. J. Wang, E. Kazyak, N. P. Dasgupta, J. Sakamoto, *Joule* **2021**, *5*, 1371.
[7] K. Takada, N. Ohta, L. Zhang, X. Xu, B. T. Hang, T. Ohnishi, M. Osada, T. Sasaki, *Solid State Ionics* **2012**, *225*, 594.
[8] K. Takada, *Acta Mater.* **2013**, *61*, 759.
[9] Y. Ren, T. Danner, A. Moy, M. Finsterbusch, T. Hamann, J. Dippell, T. Fuchs, M. Müller, R. Hoft, A. Weber, L. A. Curtiss, *Adv. Energy Mater.* **2023**, *13*, 2201939.
[10] X. Chen, J. Xie, X. Zhao, T. Zhu, *Adv. Energy Sustainability Res.* **2021**, *2*, 2000101.
[11] A. Sakuda, A. Hayashi, M. Tatsumisagoi, *Chem. Mater.* **2010**, *22*, 949.
[12] M. Ihrig, L. Y. Kuo, S. Lobe, A. M. Laptev, C. A. Lin, C. H. Tu, R. Ye, P. Kaghazchi, L. Cressa, S. Eswara, S. K. Lin, *ACS Appl. Mater. Interfaces* **2023**, *15*, 4101.
[13] R. Koerver, I. Aygün, T. Leichtweiß, C. Dietrich, W. Zhang, J. O. Binder, P. Hartmann, W. G. Zeier, J. Janek, *Chem. Mater.* **2017**, *29*, 5574.
[14] X. Han, Y. Gong, K. Fu, X. He, G. T. Hitz, J. Dai, A. Pearse, B. Liu, H. Wang, G. Rubloff, Y. Mo, V. Thangadurai, E. D. Wachsman, L. Hu, *Nat. Mater.* **2017**, *16*, 572.
[15] K. J. Kim, J. L. M. Rup, *Energy Environ. Sci.* **2020**, *13*, 4930.
[16] J. Sastre, X. Chen, A. Aribia, A. N. Tiwari, Y. E. Romanyuk, *ACS Appl. Mater. Interfaces* **2020**, *12*, 36196.
[17] K. H. Kim, Y. Iriyama, K. Yamamoto, S. Kumazaki, T. Asaka, K. Tanabe, C. A. Fisher, T. Hirayama, R. Murugan, Z. Ogumi, *J. Power Sources* **2011**, *196*, 764.
[18] G. Vardar, W. J. Bowman, Q. Lu, J. Wang, R. J. Chater, A. Aguadero, R. Seibert, J. Terry, A. Hunt, I. Waluyo, D. D. Fong, A. Jarry, E. J. Crumlin, S. L. Hellstrom, Y.-M. Chiang, B. Yildiz, *Chem. Mater.* **2018**, *30*, 6259.
[19] K. Park, B. C. Yu, J. W. Jung, Y. Li, W. Zhou, H. Gao, S. Son, *Chem. Mater.* **2016**, *28*, 8051.
[20] S. Afyon, F. Krumeich, J. L. Rupp, *J. Mater. Chem. A* **2015**, *3*, 18636.
[21] Y. Zhu, X. He, Y. Mo, *J. Mater. Chem. A* **2016**, *4*, 3253.
[22] Y. Ren, T. Liu, Y. Shen, Y. Lin, C. W. Nan, *J. Materiomics* **2016**, *2*, 256.
[23] A. Bhim, S. Laha, J. Gopalakrishnan, S. Natarajan, *Chem. - Asian J.* **2017**, *12*, 2734.
[24] K. Kusaka, K. Hagiya, M. Ohmasa, Y. Okano, M. Mukai, K. Iishi, N. Haga, *Phys. Chem. Miner.* **2001**, *28*, 150.
[25] D. L. Wood, J. P. Remeika, *J. Chem. Phys.* **1967**, *46*, 3595.
[26] D. Rettenwander, P. Blaha, R. Laskowski, K. Schwarz, P. Bottke, M. Wilkening, C. A. Geiger, G. Amthauer, *Chem. Mater.* **2014**, *26*, 2617.
[27] B. Karasulu, S. P. Emge, M. F. Groh, C. P. Grey, A. J. Morris, *J. Am. Chem. Soc.* **2020**, *142*, 3132.
[28] R. Wagner, G. J. Redhammer, D. Rettenwander, G. Tippelt, A. Welzl, S. Taibl, J. Fleig, A. Franz, W. Lottermoser, G. Amthauer, *Chem. Mater.* **2016**, *28*, 5943.
[29] G. J. Redhammer, G. Tippelt, A. Portenkirchner, D. Rettenwander, *Crystals* **2021**, *11*, 721.
[30] G. J. Redhammer, P. Badami, M. Meven, S. Ganschow, S. Berendts, G. Tippelt, D. Rettenwander, *ACS Appl. Mater. Interfaces* **2020**, *13*, 350.
[31] J. Awaka, N. Kijima, H. Hayakawa, J. Akimoto, *J. Solid State Chem.* **2009**, *182*, 2046.
[32] M. I. Demchuk, É. P. Dubrovina, N. V. Kuleshov, V. P. Mikhailov, V. A. Sandulenko, *J. Appl. Spectrosc.* **1990**, *53*, 1170.

[33] M. C. Biesinger, B. P. Payne, A. P. Grosvenor, L. W. M. Lau, A. R. Gerson, R. S. C. Smart, *Appl. Surf. Sci.* **2011**, *257*, 2717.

[34] F. C. Larcht'e, J. L. Cahn, *Acta Metall.* **1982**, *30*, 1835.

[35] D. Mazza, F. Abbatista, M. Vallino, G. Ivaldi, *J. Less-Common Met.* **1985**, *106*, 277.

[36] T. Thompson, S. Yu, L. Williams, R. D. Schmidt, R. Garcia-Mendez, J. Wolfenstine, J. L. Allen, E. Kioupakis, D. J. Siegel, J. Sakamoto, *ACS Energy Lett.* **2017**, *2*, 462.

[37] K. C. Santosh, R. C. Longo, K. Xiong, K. Cho, *Solid State Ionics* **2014**, *261*, 100.

[38] A. M. Nolan, Y. Zhu, X. He, Q. Bai, Y. Mo, *Joule* **2018**, *2*, 2016.

[39] C. Wang, K. Fu, S. P. Kammampata, D. W. McOwen, A. J. Samson, L. Zhang, G. T. Hitz, A. M. Nolan, E. D. Wachsman, Y. Mo, V. Thangadurai, *Chem. Rev.* **2020**, *120*, 4257.

[40] C. A. Geiger, E. Alekseev, B. Lazic, M. Fisch, T. Armbruster, R. Langner, M. Fechtelkord, N. Kim, T. Pettke, W. Weppner, *Inorg. Chem.* **2011**, *50*, 1089.

[41] M. Philipp, B. Gadermaier, P. Posch, I. Hanzu, S. Ganschow, M. Meven, R. Rettenwander, G. J. Redhammer, H. M. R. Wilkening, *Adv. Mater. Interfaces* **2020**, *7*, 2000450.

[42] R. Inada, K. Kusakabe, T. Tanaka, S. Kudo, Y. Sakurai, *Solid State Ionics* **2014**, *262*, 568.

[43] L. G. Harrison, *Trans. Faraday Soc.* **1961**, *57*, 1191.

[44] Y. Mishin, C. Herzig, J. Bernardini, W. Gust, *Int. Mater. Rev.* **1997**, *42*, 155.

[45] Y. Ren, E. D. Wachsman, *J. Electrochem. Soc.* **2022**, *169*, 040529.

[46] P. S. Dobal, R. S. Katiyar, M. S. Tomar, A. Hidalgo, *J. Mater. Res.* **2001**, *16*, 1.

[47] E. G. Gontier-Moya, G. Erdelyi, F. Moya, K. Freitag, *Philos. Mag. A* **2001**, *81*, 2665.

[48] Bruker, *Bruker AXS Inc*, Madison, Wisconsin, USA, **2012**.

[49] G. M. Sheldrick, *Acta Crystallogr.* **2008**, *64*, 112.

[50] L. J. Farrugia, *J. Appl. Crystallogr.* **2012**, *45*, 849.

[51] M. Schmid, H.-P. Steinrück, J. M. Gottfried, *Surf. Interface Anal.* **2014**, *46*, 505.

[52] G. Kresse, J. Hafner, *Phys. Rev. B* **1993**, *47*, 558.

[53] G. Kresse, J. Hafner, *Phys. Rev. B* **1994**, *49*, 285.

[54] G. Kresse, J. Furthmüller, *Phys. Rev. B* **1996**, *54*, 11169.

[55] P. E. Blochl, *Phys. Rev. B* **1994**, *50*, 17953.

[56] J. Perdew, K. Burke, M. Ernzerhof, *Phys. Rev. Lett.* **1996**, *77*, 3865.

[57] J. Heyd, G. E. Scuseria, M. Ernzerhof, *J. Chem. Phys.* **2003**, *118*, 8207.

[58] A. V. Krukau, O. A. Vydrov, A. F. Izmaylov, G. E. Scuseria, *J. Chem. Phys.* **2006**, *125*, 224106.